^{16}C inelastic scattering studied with the microscopic coupled-channels method

M. Takashina,[1,*] Y. Kanada-En'yo,[2] and Y. Sakuragi[1,3]

^{1}*RIKEN, Hirosawa 2-1, Wako, Saitama 351-0198, Japan*

^{2}*Institute of Particle and Nuclear Studies, High Energy Accelerator Research Organization, Ibaraki 305-0801, Japan*

^{3}*Department of Physics, Osaka City University, Osaka 558-8585, Japan*

In order to test the ^{16}C internal wave function, we perform microscopic coupled-channels (MCC) calculations of the ^{16}C($0_1^+ \rightarrow 2_1^+$) inelastic scattering by a ^{208}Pb target at $E/A = 52.7$ MeV using the antisymmetrized molecular dynamics (AMD) wave functions of ^{16}C, and compare the calculated differential cross sections with the measured ones. The MCC calculations with AMD wave functions reproduce the experimental data fairly well, although they slightly underestimate the magnitude of the cross sections. The absolute magnitude of calculated differential cross sections is found to be sensitive to the neutron excitation strength. We prove that the MCC method is a useful tool for connecting the inelastic scattering data with the internal wave functions.

I. INTRODUCTION

Recently, opposite deformations between proton and neutron densities in C isotopes were theoretically suggested [1,2] by the method of antisymmetrized molecular dynamics (AMD): The proton density has an oblate deformation, while the neutron density has a prolate deformation, and the symmetry axis of the proton is perpendicular to that of the neutron in ^{10}C and ^{16}C. Based on this picture, the author also gave a qualitative explanation [3] for an unusually small electric transition strength $B(E2; 2_1^+ \rightarrow 0_1^+) = 0.63 \pm 0.19 \, e^2 \, \text{fm}^4$ in ^{16}C, which is derived from a lifetime measurement [4]. According to Ref. [3], the 2_1^+ state is a rotational excited state, and the rotational axis is perpendicular to the neutron symmetry axis. In this excitation mechanism, the proton transition strength is reduced due to the difference of deformation between the proton and neutron distributions mentioned above, and therefore, the $0_1^+ \rightarrow 2_1^+$ transition is dominated by the neutron excitation.

In order to search for the possible difference between proton and neutron contributions to excitation of the 2_1^+ state in ^{16}C, an inelastic scattering experiment of ^{16}C on a ^{208}Pb target was performed [5] applying the Coulomb-nuclear interference method. The analysis was carried out by using the deformed potential model, and the proton and neutron transition matrix elements M_p and M_n were extracted. In Ref. [5], it is mentioned that the experimental transition probability is inconsistent with theoretical ones (the AMD, extended AMD, and shell-model calculations are cited). However, the phenomenological analysis done in Ref. [5] contains some assumptions, and hence, it seems inappropriate to compare the M_p and M_n values evaluated in Ref. [5] with those calculated theoretically.

To test the ^{16}C internal wave function, we should directly link the cross section with the wave function, by calculating the differential cross sections of the inelastic

scattering of ^{16}C on the ^{208}Pb target with the microscopic coupled-channels (MCC) method, and compare the calculated result with the experimental reaction data measured in Ref. [5].

The MCC method has been applied for studying reactions of stable nuclei, such as ^{6,7}Li and ^{9}Be elastic and inelastic scattering [6,7], the resonance reactions of the ^{12}C+^{12}C system leading to inelastic [8,9] and ^{8}Be+^{16}O α-transferred channels [10], the rainbow scattering of the ^{16}O+^{16}O system [11], etc., adopting the microscopic cluster model wave functions of ^{6,7}Li [6], ^{9}Be [12], ^{12}C [13], and ^{16}O [14]. Because the microscopic cluster model wave functions well reproduce the measured charge form factors of not only the elastic electron-scattering but also the inelastic one, the wave functions are reliable and suitable for studying nuclear reaction mechanisms. The MCC calculations successfully reproduce the experimental reaction data. The reliability of the method has already been established. Hence, we think it is possible to examine inversely the validity of calculated internal wave functions by comparing the result of MCC with experimental reaction data.

In this paper, we adopt the AMD internal wave function of ^{16}C. The reasons we think it is worthy to test the validity of the AMD wave function in the present study are as follows. (1) Because no inert cores and no clusters are assumed, the AMD wave function is flexible. Therefore, AMD is suited for structural study of general unstable nuclei. The applicability has been proved in many works [2]. (2) Deformations of proton and neutron densities are obtained dynamically. In other words, electromagnetic transition probability can be calculated without introducing effective charge. (3) In AMD, it is easy to carry out the spin-parity projection, which is necessary for microscopic calculation of transition density.

It should be noted that any nuclear structure models are applicable to MCC, if the diagonal density and transition densities to excited states can be calculated from a model wave function that gives no spurious center-of-mass component. In the next section, we briefly describe the MCC method. A more detailed description is given in Refs. [9,11].

*Email address: takasina@rarfaxp.riken.jp

II. FORMALISM

A. Coupled-channels formalism

The coupled-channels equation describing the collision of two nuclei for a total angular momentum of the system J is written as

$$\left[T_R + U^{(J)}_{\alpha L, \alpha L}(R) - E_\alpha\right]\chi^{(J)}_{\alpha L}(R)$$
$$= -\sum_{(\alpha'L')\neq(\alpha L)} U^{(J)}_{\alpha L, \alpha' L'}(R)\chi^{(J)}_{\alpha' L'}(R), \qquad (1)$$

where T_R denotes the kinetic-energy operator, and α and L denote a channel and the orbital angular momentum associated to the relative coordinate $\boldsymbol{R}$, respectively. In the present study, we take into account the elastic and ^{16}C excitation channels, while only the ground state (0^+) is considered for the target ^{208}Pb nucleus. Thus, the channel α is designated by the spin I and the excitation energy ϵ_α of ^{16}C. E_α represents the center-of-mass energy for the projectile-target relative motion in channel α ($E_\alpha = E_{\text{c.m.}} - \epsilon_\alpha$). $\chi^{(J)}_{\alpha' L'}(R)$ is the relative wave function and is obtained by solving Eq. (1) numerically.

In Eq. (1), $U^{(J)}_{\alpha L, \alpha' L'}(R)$ represents the diagonal $(\alpha, L) = (\alpha', L')$ or the coupling $(\alpha, L) \neq (\alpha', L')$ potential, which is composed of the nuclear part $V^{N(J)}_{\alpha L, \alpha' L'}(R)$ and the Coulomb part $V^{C(J)}_{\alpha L, \alpha' L'}(R)$. The nuclear part is given by the double-folding model and defined as

$$V^{N(J)}_{\alpha L, \alpha' L'}(R) = \frac{1}{4\pi}\sum_\lambda \hat{L}\hat{L}' i^{L-L'}(-1)^{J-I} W(ILI'L'; J\lambda)$$

$$\times (L0L'0|\lambda 0)\frac{\hat{I}}{\hat{\lambda}}\int d\hat{\boldsymbol{R}}\, d\boldsymbol{r}_1\, d\boldsymbol{r}_2\{v_{00}(\boldsymbol{x})[\rho^{n(\lambda)}_{II'}(r_1)$$
$$+ \rho^{p(\lambda)}_{II'}(r_1)][\rho^{n(0)}_{00}(r_2) + \rho^{p(0)}_{00}(r_2)] + v_{01}(\boldsymbol{x})$$
$$\times [\rho^{n(\lambda)}_{II'}(r_1) - \rho^{p(\lambda)}_{II'}(r_1)][\rho^{n(0)}_{00}(r_2) - \rho^{p(0)}_{00}(r_2)]\}$$
$$\times [Y_\lambda(\hat{\boldsymbol{r}}_1) \otimes Y_\lambda(\hat{\boldsymbol{R}})]_{00}$$
$$(\boldsymbol{x} = \boldsymbol{r}_1 + \boldsymbol{R} - \boldsymbol{r}_2), \qquad (2)$$

where $W(ILI'L'; J\lambda)$ represents the ordinary Racah coefficient, and $\hat{I}$ is $\sqrt{2I+1}$. $\rho^{p(\lambda)}_{II'}(r_1)$ and $\rho^{n(\lambda)}_{II'}(r_1)$ $[\rho^{p(0)}_{00}(r_2)$ and $\rho^{n(0)}_{00}(r_2)]$ are the radial components of the proton and neutron transition densities of ^{16}C (^{208}Pb), respectively, which are mentioned in the next subsection in detail. $v_{00}(\boldsymbol{x})$ represents the spin- and isospin-scalar ($S = T = 0$) component of an effective nucleon-nucleon interaction, while $v_{01}(\boldsymbol{x})$ represents the spin-scalar, isospin-vector ($S = 0, T = 1$) component. For this effective interaction, we adopt the DD$M3Y$ (density-dependent Michigan three-range Yukawa) [15,16], which is defined by

$$v_{00(01)}(E, \rho; \boldsymbol{r}) = g_{00(01)}(E, \boldsymbol{r})f(E, \rho), \qquad (3)$$

where $\boldsymbol{r}$ is the internucleon separation, and $f(E, \rho)$ is a density-dependent factor

$$f(E, \rho) = C(E)[1 + \alpha(E)e^{-\beta(E)\rho}]. \qquad (4)$$

Here, E denotes an incident energy per nucleon in the laboratory system. The coefficients $C(E)$, $\alpha(E)$, and $\beta(E)$ in the density-dependent factor $f(E, \rho)$ were determined at each energy by fitting a volume integral of the $v_{00}(E, \rho; \boldsymbol{r})$ to

the real part of the optical potential felt by a nucleon in the nuclear matter [17]. $g_{00(01)}(E, \boldsymbol{r})$ in Eq. (3) is the original $M3Y$ interaction [18,19]

$$g_{00}(E, \boldsymbol{r}) = 7999\frac{e^{-4r}}{4r} - 2134\frac{e^{-2.5r}}{2.5r} + \hat{J}_{00}(E)\delta(\boldsymbol{r})\text{ MeV}, \qquad (5)$$

with

$$\hat{J}_{00}(E) = -276(1 - 0.005E)\text{ MeV fm}^3, \qquad (6)$$

and

$$g_{01}(E, \boldsymbol{r}) = -4886\frac{e^{-4r}}{4r} + 1176\frac{e^{-2.5r}}{2.5r} + \hat{J}_{01}(E)\delta(\boldsymbol{r})\text{ MeV}, \qquad (7)$$

with

$$\hat{J}_{01}(E) = 228.4(1 - 0.005E)\text{ MeV fm}^3. \qquad (8)$$

The units for E and r are MeV/nucleon and fm, respectively.

The Coulomb part $V^{C(J)}_{\alpha L, \alpha' L'}(R)$ is also given by the double-folding model. The double-folded Coulomb potential is written in the same form as Eq. (2), by replacing the neutron densities and the nucleon-nucleon interaction as

$$\rho^{n(\lambda)}_{II'}(r_1), \rho^{n(0)}_{00}(r_2) \to 0, \quad v_{00}(\boldsymbol{x}) \to \frac{e^2}{x}, \quad v_{01}(\boldsymbol{x}) \to 0.$$

Since DD$M3Y$ has no imaginary part, we add the imaginary potential $W^{N(J)}_{\alpha L, \alpha' L'}(R)$ to the nuclear part, which is assumed as $W^{N(J)}_{\alpha L, \alpha' L'}(R) = N_I V^{N(J)}_{\alpha L, \alpha' L'}(R)$, where N_I is the only phenomenological parameter of the present MCC formalism. The simple assumption for the imaginary part should be valid in the present case, since we only discuss the cross sections at very forward scattering angles, which are not sensitive to the detail of the shape of the potential in the whole radial range. Hence, the interaction potential has the form

$$U^{N(J)}_{\alpha L, \alpha' L'}(R) = (1 + iN_I)V^{N(J)}_{\alpha L, \alpha' L'}(R) + V^{C(J)}_{\alpha L, \alpha' L'}(R). \qquad (9)$$

B. Transition density

The diagonal or transition density of a proton at a position $\boldsymbol{r}$ with respect to the center of mass of the nucleus can be expanded into multipole components

$$\rho^P_{I\nu, I'\nu'}(\boldsymbol{r}) = \left\langle \psi^p_{I\nu}(\xi)\Big| \sum_{i=1}^{Z} \delta(\boldsymbol{r} - \boldsymbol{r}_i)\Big|\psi^p_{I'\nu'}(\xi)\right\rangle$$
$$= \sum_{\lambda,\mu}(I'\nu'\lambda\mu|I\nu)\rho^{p(\lambda)}_{II'}(r)Y^*_{\lambda\mu}(\hat{\boldsymbol{r}}), \qquad (10)$$

where $\psi^p_{I\nu}(\xi)$ represents the proton wave function in the nucleus. $\rho^{p(\lambda)}_{II'}(r)$ represents the radial component of the transition density, which is used in Eq. (2). The radial component of the neutron transition density $\rho^{n(\lambda)}_{II'}(r)$ is obtained in the same manner as the proton case in terms of the neutron wave function $\psi^n_{I\nu}(\xi)$. The proton or neutron matrix element of rank λ is defined as

$$M^{(\lambda)}_\tau(I' \to I) = \hat{I}\int \rho^{\tau(\lambda)}_{II'}(r)\, r^{\lambda+2}dr, \qquad (11)$$

TABLE I. $B(E2)$, $M_p^{(2)}$, and $M_n^{(2)}$ values of ^{16}C calculated by AMD, in which the strength of the spin-orbit force is set to (i) $u_{ls} = 900$ MeV, (ii) $u_{ls} = 1500$ MeV, and (iii) $u_{ls} = 2000$ MeV. The experimental data of $B(E2)$ is taken from Ref. [4].

	(i)	(ii)	(iii)	exp.
$B(E2; 2_1^+ \rightarrow 0_1^+)(e^2 \, \text{fm}^4)$	1.9	1.4	0.9	0.63 ± 0.19
$M_p^{(2)}(2_1^+ \rightarrow 0_1^+)(\text{fm}^2)$	3.1	2.6	2.2	–
$M_n^{(2)}(2_1^+ \rightarrow 0_1^+)(\text{fm}^2)$	13.0	12.2	8.9	–

where τ represents p or n. The proton matrix element is related with the electric transition strength $B(E\lambda)$ as

$$B(E\lambda; I' \rightarrow I) = \frac{\left| M_p^{(\lambda)}(I' \rightarrow I) \right|^2}{\hat{I}'^2} e^2. \qquad (12)$$

Here, we use the AMD wave function for $\psi_{I\nu}^p(\xi)$ and $\psi_{I\nu}^n(\xi)$ to calculate the transition densities defined in Eq. (10). We consider the ground state (0_1^+) and the first excited 2_1^+ state. In Ref. [3], two versions of the ^{16}C internal wave function are obtained in the variation before projection (VBP) formalism, changing the strength of the spin-orbit force: (i) $u_{ls} = 900$ MeV and (ii) $u_{ls} = 1500$ MeV. The $B(E2)$ values as well as the $M_p^{(2)}$ and $M_n^{(2)}$ ones obtained with AMD wave functions (i) and (ii) are summarized in Table I with the experimental data of $B(E2)$. With spin-orbit forces (i) and (ii), the AMD calculation reproduces well the systematic behavior of the $B(E2)$ value and the root-mean-square radius of the C isotopes as shown in Ref. [3]. In particular, the systematic feature that the $B(E2)$ value of ^{16}C is abnormally small compared with other C isotopes (^{10}C, ^{12}C, and ^{14}C) is well reproduced by AMD with spin-orbit forces (i) and (ii), although the $B(E2)$ value of ^{16}C is slightly overestimated. In addition to the above two, we also use the AMD wave function for which the strength of the spin-orbit force is set to (iii) $u_{ls} = 2000$ MeV so as to reduce the $B(E2)$ value and to be close to the experimental value. The $B(E2)$ value, as well as the $M_p^{(2)}$ and $M_n^{(2)}$ ones of case (iii), is also shown in Table I. One might think that case (iii) gives the best wave function. However, increasing the strength of the spin-orbit force to reduce the $B(E2)$ value of only ^{16}C, as done in case (iii), may lead to an unrealistic situation, because the systematic behavior of the other C isotopes is not reproduced with such strong spin-orbit force. Hereafter, we refer to the three versions of AMD wave function as AMD(i), AMD(ii), and AMD(iii).

Figure 1 shows the radial components of the diagonal and transition densities obtained with AMD(i). In the upper panel (A), the $\lambda = 0$ components of the diagonal density are shown. The solid curves represent the proton and neutron densities of the ground state (0_1^+), and the dashed curves represent those of the 2_1^+ state. It is found that the shape of the 2_1^+ diagonal densities is almost the same as the shape of those of 0_1^+, except for the region around the origin. The proton density of the 2_1^+ state is almost identical to that of the 0_1^+ state, and the difference cannot be seen Fig. 1. In the lower panel (B), the $\lambda = 2$ components of the diagonal and transition density are shown. The dotted and solid
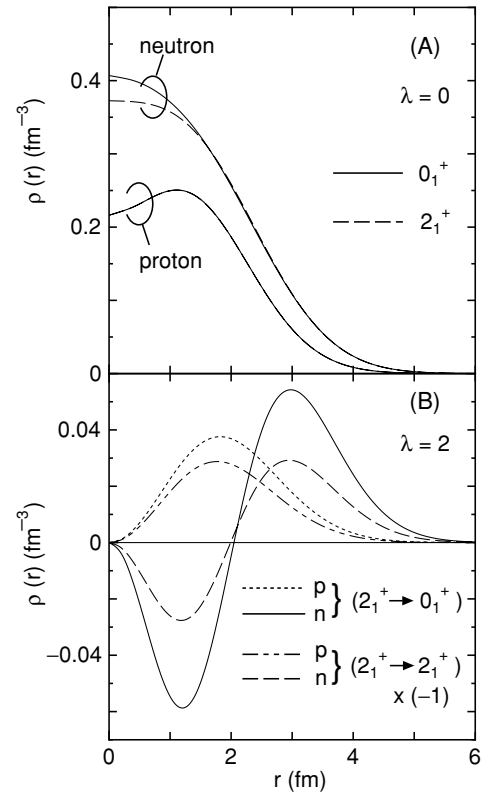

FIG. 1. The radial components of the diagonal and transition densities obtained with AMD(i) for ^{16}C. (A) $\lambda = 0$ component. The solid curves represent the proton and neutron diagonal densities of the ground state (0_1^+), while the dashed curves represent those of the 2_1^+ state. The proton density of the 2_1^+ state is almost identical to that of the 0_1^+ state, and the difference cannot be seen in the figure. (B) $\lambda = 2$ component. The dotted and solid curves represent the proton and neutron transition densities, respectively, from 2 to 0_1^+. The double-dot-dashed and dashed curves represent the $\lambda = 2$ components of the proton and neutron diagonal densities, respectively, for the 2_1^+ state. These two curves are displayed with opposite sign.

curves represent the proton and neutron transition densities, respectively, for the $2_1^+ \rightarrow 0_1^+$ transition. The transition is found to be dominated by the neutron component, especially in the surface region. The double-dot-dashed and dashed curves are the $\lambda = 2$ components of the 2_1^+ diagonal density for the proton and neutron, respectively. These two curves are displayed with opposite sign in Fig. 1. The shapes of the double-dot-dashed and dashed curves are similar to the dotted and solid curves, respectively. It should be noted that the proton part of the $\lambda = 2$ component of the diagonal density is proportional to the electric quadrupole moment of the 2_1^+ state. We neglect the $\lambda = 4$ component of the 2_1^+ diagonal density, because this component is very small and is expected to have a small contribution to the inelastic scattering.

In Fig. 2(A), the proton transition density of AMD(i) (solid curve) is compared with those of AMD(ii) and AMD(iii),
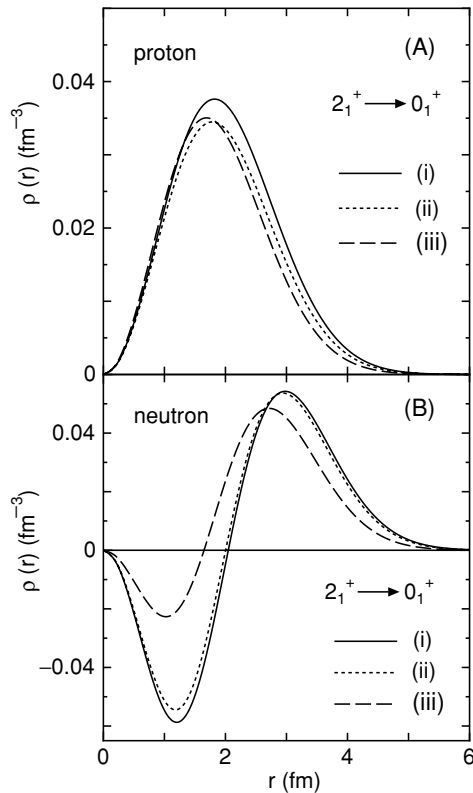
FIG. 2. Comparison of the proton (A) and neutron (B) transition densities for $2_1^+ \rightarrow 0_1^+$. The solid, dotted, and dashed curves represent the transition densities of AMD(i), AMD(ii), and AMD(iii), respectively. The solid curves in (A) and (B) are the same as the dotted and solid curves in Fig. 1(B), respectively.

FIG. 3. The diagonal (A) and coupling (B) potentials of the ^{16}C+^{208}Pb system calculated with AMD(i) are represented by the solid curves. The dotted and dashed curves are the contributions of the proton and neutron components of ^{16}C, respectively, where both the proton and neutron components of ^{208}Pb(0_1^+) are included.

which are represented by the dotted and dashed curves, respectively. The transition densities of AMD(ii) and AMD(iii) are smaller than that of AMD(i), and the transition density of AMD(iii) is slightly shifted to the small r side. The difference of the proton transition density causes the difference of the electric transition strength, as shown in Table I. In Fig. 2(B), the neutron transition densities of AMD(i), (ii), and (iii) are shown by the solid, dotted, and dashed curves, respectively. Although the overall shapes of the transition densities of (i) and (ii) are almost the same, the magnitudes are found to be slightly different. The magnitude of the transition density of AMD(iii) is suppressed when it is compared with those of (i) and (ii), especially in the inner region.

The proton density distribution of the ^{208}Pb nucleus is obtained by unfolding the charge density [20], which was obtained by a model-independent analysis of an electron scattering experiment, with the realistic proton charge form factor [21]. The neutron density distribution is obtained by assuming that the shape of the neutron density is the same as that of proton one, namely $\rho_n(\boldsymbol{r}) = (N/Z)\rho_p(\boldsymbol{r})$. This assumption is known to be valid for stable nuclei.

In the next section, we show the results of the MCC calculation using the AMD transition densities described above.
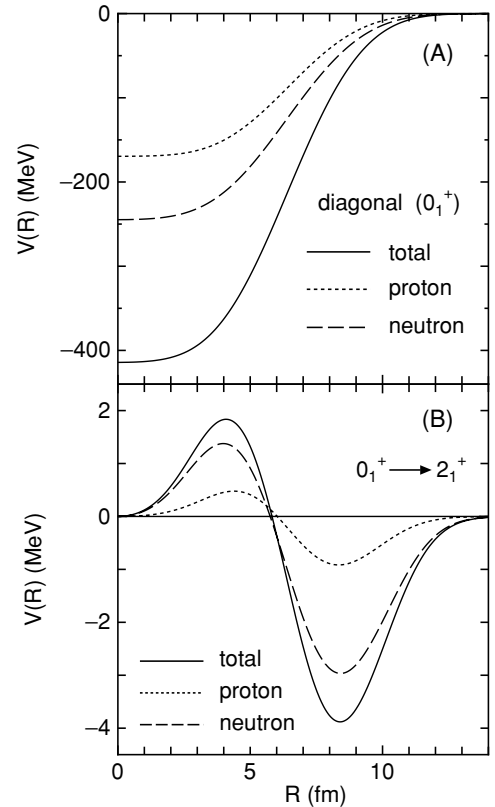
III. RESULTS

In Fig. 3, we show the double-folding model potential using the densities obtained by AMD(i) described in Sec. II B. The solid curve represents the nuclear potential Eq. (2). The dotted and dashed curves are the contributions of proton and neutron components of ^{16}C, respectively, where both the proton and neutron components of ^{208}Pb(0_1^+) are included. In Fig. 3(A), the diagonal potential of the ^{16}C(0_1^+)+^{208}Pb elastic channel is shown. Since the diagonal density of the 2_1^+ state in ^{16}C resembles closely that of the 0_1^+ state as shown in Fig. 1(A), the diagonal potential of ^{16}C(2_1^+)+^{208}Pb is almost the same as that of ^{16}C(0_1^+)+^{208}Pb, and therefore, it is not shown here. In Fig. 3(B), the coupling potential of ^{16}C($0_1^+ \rightarrow 2_1^+$)+^{208}Pb is shown. It is found that the neutron component has a dominant contribution to the total potential, especially in the vicinity of the strong absorption radius $r_{\mathrm{SA}} \sim 11$ fm.

In order to see the effect of the isovector component, we also decompose the diagonal and coupling potentials into the isoscalar and isovector components. The result is shown in Fig. 4. The solid curves are the same as the solid ones in Fig. 3, and the dotted and dashed curves are the isoscalar (IS) and isovector (IV) components, respectively. Compared with the isoscalar component, the magnitude of the isovector component is about 5%, and the sign is opposite. The 5%
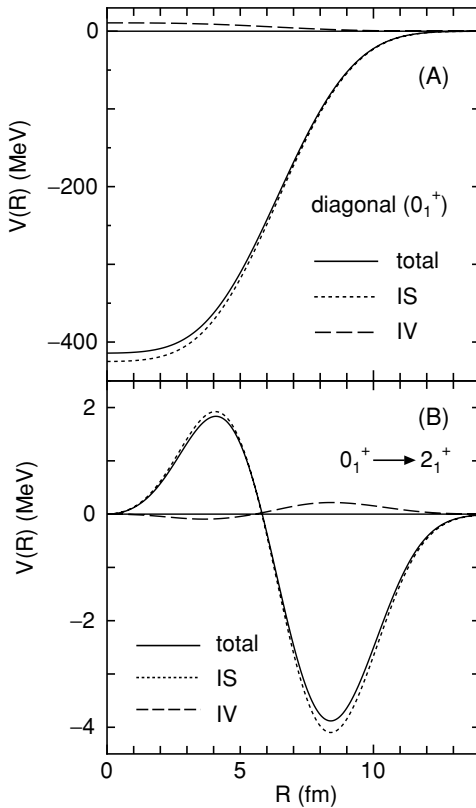
FIG. 4. The isoscalar (dotted) and isovector (dashed) components of the diagonal (A) and coupling (B) potentials. The solid curves are the same as those in Fig. 3.

FIG. 5. Angular distribution of $^{16}C(0_1^+ \to 2_1^+)$ inelastic scattering on a ^{208}Pb target at $E/A = 52.7$ MeV. The crosses are the experimental data, and the solid curve is the result of our calculation. The dotted and dashed curves are the nuclear and Coulomb components, respectively.

reduction of the coupling potential leads to about a 10% reduction of the inelastic scattering cross sections and is not negligible in the present case. Therefore, we include the isovector component throughout the present calculations.

We perform a coupled-channels calculation using the diagonal and coupling potentials shown in Fig. 3. Because of the high incident energy, the coupled-channels equations are solved numerically with the relativistic kinematics, which has a non-negligible effect at forward-angle cross sections. The parameter for the imaginary potential N_I is set to 1.2. Following the procedure of Ref. [5], the calculated cross sections are smoothed by Gaussian functions according to the experimental angular uncertainty of $0.28°$. The result is shown in Fig. 5. The differential cross sections are shown as a function of scattering angle θ in the laboratory system. The crosses are the experimental data [5], and the solid curve represents the result of the coupled-channels calculation. It is found that the MCC calculation with AMD(i) reproduces the experimental data fairly well, although it slightly underestimates the magnitude of the cross sections at large angles. While the oscillatory shape of the angular distribution is formed by interference between the nuclear and Coulomb components, which are represented by the dotted and dashed curves, respectively, in Fig. 5, the average strength of the calculated cross section is determined by the nuclear excitation. Particularly, the neutron component dominates the nuclear excitation as understood from Fig. 3(B). Therefore, the
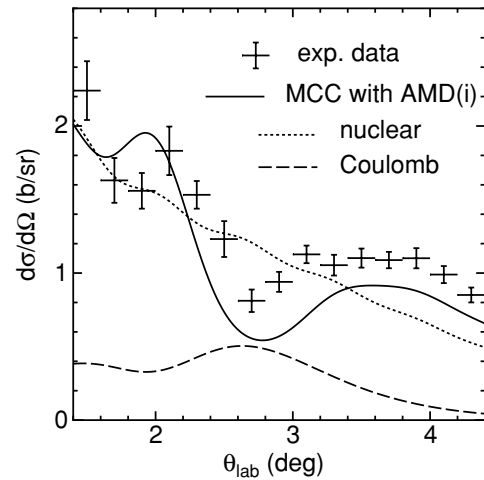
present result indicates that AMD(i) slightly underestimates the neutron excitation strength by about 10%, while it overestimates the proton excitation strength as shown in Table I.

The parameter N_I cannot be determined theoretically in the present MCC framework. In order to see the N_I dependence of the calculated result, we perform the same calculation with different N_I values. The results are shown in Fig. 6. The dotted, dashed, solid, dot-dashed, and double-dot-dashed curves are the results of the MCC calculations with $N_I = 1.0, 1.1, 1.2, 1.3,$ and 1.4, respectively. It is seen that N_I dependence is very weak, although the cross sections at very forward angles change slightly with N_I. The angular distribution around $\theta_{lab} = 3$–4 deg is seen to be independent of the N_I value. Because the calculation with $N_I = 1.2$
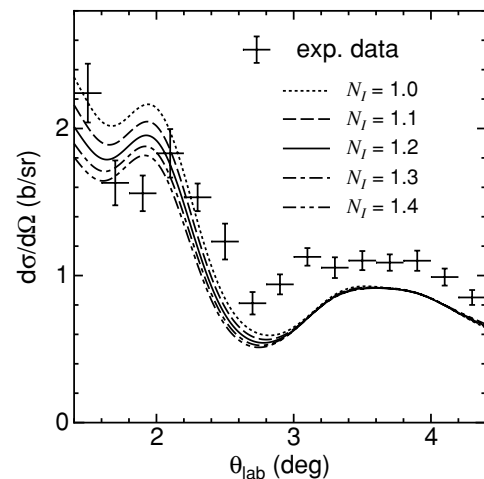

FIG. 6. N_I dependence of the calculated differential cross sections. The dotted, dashed, solid, dot-dashed and double-dot-dashed curves are the results of the MCC calculations with $N_I = 1.0, 1.1, 1.2, 1.3,$ and 1.4, respectively.
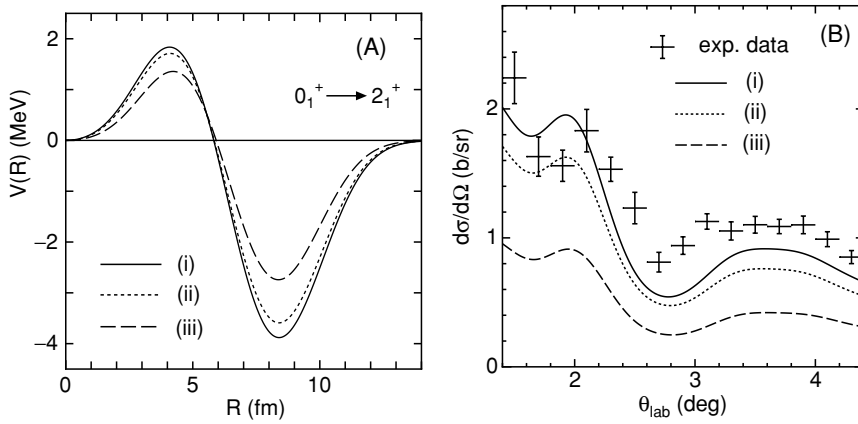
FIG. 7. (A) The coupling potentials calculated with AMD(i), (ii), and (iii) are shown by the solid, dotted, and dashed curves, respectively. (B) The results of the MCC calculations with AMD(i), (ii), and (iii) are shown by the solid, dotted, and dashed curves, respectively. The crosses are the experimental data.

reproduces the shape of the data a little better than others, we choose $N_I = 1.2$ in the present calculation.

Next, we perform the MCC calculations using AMD(ii) and (iii). In Fig. 7(A), the coupling potential with AMD(i) represented by the solid curve is compared with those with (ii) and (iii), which are represented by the dotted and dashed curves, respectively. One can see that the strength of the coupling potential is almost proportional to the $M_p^{(2)} + M_n^{(2)}$ value: 16.1 fm^2 for (i), 14.8 fm^2 for (ii), and 11.1 fm^2 for (iii). The results of the MCC calculations with AMD(ii) and (iii) are shown in Fig. 7(B) by the dotted and dashed curves, compared with the result of AMD(i) shown by the solid curve, which is the same as that in Fig. 5, and the experimental data. As expected from the strength of the coupling potential, the differential cross sections with AMD(ii) are slightly smaller than those calculated with AMD(i), and those with AMD(iii) severely underestimate the magnitude of the measured cross sections. The magnitude of the differential cross section of inelastic scattering directly reflects the electric and hadronic transition strength of the ^{16}C nucleus. For AMD(iii), the proton transition seems good because it gives a $B(E2)$ value that is close to the measured one. However, the nuclear excitation strength of (iii) is too small, as shown in Fig. 7(B). Since the nuclear excitation is dominated by the neutron component, this result indicates that AMD(iii) fails to describe the neutron excitation correctly. This fact cannot be determined from the

experimental data of the electromagnetic probe. Therefore, we think it is very important that the internal wave function of a nucleus obtained theoretically be tested by the experimental data of a hadronic probe to investigate the behavior of the neutron component.

For further investigation, it is very interesting to analyze the experimental data of the ^{16}C inelastic scattering on a proton target measured at RIKEN [22], which is more sensitive to the neutron excitation.

Finally, we see how the angular distribution changes if the symmetry axis of the proton is aligned to that of the neutron. In the original AMD wave function, the symmetry axis of the proton is perpendicular to that of the neutron. We artificially make the aligned proton density from the AMD wave function (ii) by rotating the proton wave function to set its symmetry axis to be parallel to the neutron one. The aligned proton density is shown in Fig. 8(A) by the dotted curve. The solid curve is the neutron transition density, which is the same as the dotted curve in Fig. 2(B). The proton transition density has the sign opposite to the neutron one in the surface region. The result of the MCC calculation using this aligned proton transition density is shown in Fig. 8(B). It is found that the calculated angular distribution is out of phase compared with the experimental data. This result indicates that the proton transition density should have the same sign as the neutron transition density in the surface region.
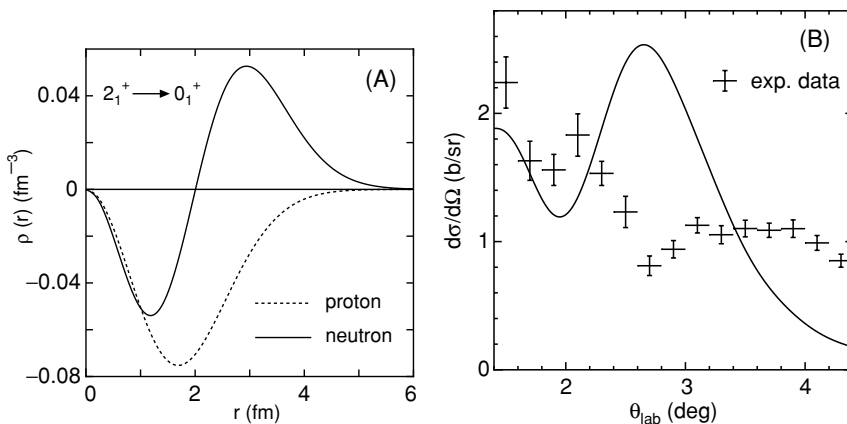

FIG. 8. (A) The proton transition density when the symmetry axis is artificially rotated to be parallel to the neutron one is shown by the dotted curve. The neutron transition density shown by the solid curve is the same as the dotted curve in Fig. 2(B). (B) The result of the MCC calculation when the aligned proton density shown in (A) is used.

IV. SUMMARY AND CONCLUSION

In order to test the ^{16}C internal wave function, we studied the ^{16}C($0_1^+ \to 2_1^+$) inelastic scattering on a ^{208}Pb target at $E/A =$ 52.7 MeV [5] by the microscopic coupled-channels (MCC) method using the internal wave function of the ^{16}C nucleus obtained by antisymmetrized molecular dynamics (AMD) [3]. In Ref. [3], two versions of wave function are obtained with the strength of spin-orbit force: (i) $u_{\ell s} = 900$ MeV and (ii) $u_{\ell s} = 1500$ MeV. It was shown in Ref. [3] that these AMD calculations reproduced the systematic behavior of the $B(E2)$ value and the root-mean-square (RMS) radius of C isotopes. The MCC calculations using these wave functions of ^{16}C reproduce well the measured differential cross sections, although they slightly underestimate the magnitude of the cross sections at large angles. In particular, the shape is rather well reproduced around $\theta_{\mathrm{lab}} = 3$–4 deg, where the angular distribution is independent of the strength parameter N_I of the imaginary potential. While the shape of the differential cross section due to the interference between the nuclear and Coulomb excitation components is sensitive to the strength of the proton excitation, the magnitude of the cross section is sensitive to the strength of neutron excitation, because the nuclear excitation is dominated by the neutron excitation in the present case. Therefore, we can conclude that the AMD wave function of (i) predicts the neutron excitation strength of ^{16}C reasonably well, although the strength may be slightly underestimated by about 10%.

We also performed a coupled-channels calculation using the AMD wave function, for which the strength of the spin-orbit force is set to (iii) $u_{\ell s} = 2000$ MeV. Although this wave function gives a $B(E2)$ value of ^{16}C close to the measured one, the systematic behavior of $B(E2)$ and the RMS radius of the other C isotopes failed to be reproduced due to the unrealistic strength of the spin-orbit force. The MCC calculation using AMD(iii) severely underestimates the differential cross sections, which indicates that the neutron excitation is not properly described when the spin-orbit force (iii) is used. It can be said that testing the validity of the calculated wave function with only the electromagnetic experimental data, such as the $B(E2)$ value, may be insufficient. Especially for neutron-rich nuclei, it is expected that the proton density is significantly different from the neutron one. Therefore, we think it is very important that the internal wave functions of a nucleus obtained by any nuclear structure theory be tested by not only the experimental data of an electromagnetic probe but also those of a hadronic probe, particularly to investigate the behavior of the neutron component, as done in the present paper.

We showed that the MCC calculation is a useful tool to link the inelastic scattering data with the internal wave functions obtained theoretically. Note that since the diagonal density is also reflected by the behavior of the calculated differential cross section through the diagonal potential as the distorting effect, the overall feature of diagonal and transition densities of a nucleus can be tested consistently with this procedure. Nuclear reaction data themselves are available for nuclear structure study as are the RMS radius, the electromagnetic transition strength, the charge form factor, etc., by applying the MCC method.

[1] Y. Kanada-En'yo and H. Horiuchi, Phys. Rev. C **55**, 2860 (1997).

[2] Y. Kanada-En'yo and H. Horiuchi, Prog. Theor. Phys. Suppl. **142**, 205 (2001).

[3] Y. Kanada-En'yo, Phys. Rev. C **71**, 014310 (2005).

[4] N. Imai *et al.*, Phys. Rev. Lett. **92**, 062501 (2004).

[5] Z. Elekes *et al.*, Phys. Lett. **B586**, 34 (2004).

[6] Y. Sakuragi, M. Yahiro, and M. Kamimura, Prog. Theor. Phys. Suppl. **89**, 136 (1986).

[7] Y. Hirabayashi, S. Okabe, and Y. Sakuragi, Phys. Lett. **B221**, 227 (1989).

[8] Y. Hirabayashi, Y. Sakuragi, and Y. Abe, Phys. Rev. Lett. **74**, 4141 (1995).

[9] M. Ito, Y. Sakuragi, and Y. Hirabayashi, Phys. Rev. C **63**, 064303 (2001); M. Ito, Y. Hirabayashi, and Y. Sakuragi, *ibid.* **66**, 034307 (2002).

[10] M. Takashina, M. Ito, Y. Kudo, S. Okabe, and Y. Sakuragi, Phys. Rev. C **67**, 014609 (2003).

[11] M. Katsuma, Y. Sakuragi, S. Okabe, and Y. Kondō, Prog. Theor. Phys. **107**, 377 (2002).

[12] S. Okabe and Y. Abe, Prog. Theor. Phys. **61**, 1049 (1979).

[13] Y. Fukushima and M. Kamimura, in *Proceedings of the International Conference on Nuclear Structure*, edited by T. Marumori [J. Phys. Soc. Jpn. Suppl.] **44** (1978), p. 225.

[14] S. Okabe, in *Tours Symposium on Nuclear Physics II*, edited by H. Utsunomiya *et al.* (World Scientific, Singapore, 1995), p. 112.

[15] A. M. Kobos *et al.*, Nucl. Phys. **A384**, 65 (1982); **A425**, 205 (1984).

[16] M. El-Azab and G. R. Satchler, Nucl. Phys. **A438**, 525 (1985).

[17] J. P. Jeukenne, A. Lejeune, and C. Mahaux, Phys. Rev. C **16**, 80 (1977).

[18] G. Bertsch, J. Borysowicz, H. McManus, and W. G. Love, Nucl. Phys. **A284**, 399 (1977).

[19] G. R. Satchler and W. G. Love, Phys. Rep. **55**, 183 (1979).

[20] H. de Vries, C. W. de Jager, and C. de Vries, At. Data Nucl. Data Tables **36**, 495 (1987).

[21] T. Janssens *et al.*, Phys. Rev. **142**, 922 (1966).

[22] H. J. Ong *et al.*, submitted to Phys. Rev. C.